Chinese Chemical Letters 33 (2022) 5132–5136

Contents lists available at ScienceDirect

Chinese Chemical Letters

journal homepage: www.elsevier.com/locate/cclet

Illuminations for constructions of scintillating lanthanide–organic complexes in sensitive X-ray detection and high-resolution radiative imaging

Juan Gao[a,b,c], Jian Lu[a,b,d,*], Baoyi Li[a,b], Wenfei Wang[a,b,c], Meijuan Xie[a,b], Shuaihua Wang[a,b], Fakun Zheng[a,b,*], Guocong Guo[a,b]

[a] State Key Laboratory of Structural Chemistry, Fujian Institute of Research on the Structure of Matter, Chinese Academy of Sciences, Fuzhou 350002, China
[b] Fujian Science and Technology Innovation Laboratory for Optoelectronic Information of China, Fuzhou 350108, China
[c] University of Chinese Academy of Sciences, Beijing 100039, China
[d] State Key Laboratory of Quality Research in Chinese Medicine, Institute of Chinese Medical Sciences, University of Macau, Macau SAR 999078, China

ARTICLE INFO

Article history:
Received 11 January 2022
Revised 18 March 2022
Accepted 20 March 2022
Available online 23 March 2022

Keywords:
Scintillating materials
Metal–organic frameworks
Lanthanide coordination compounds
X-ray detection
X-ray imaging

ABSTRACT

X-ray detection and imaging *via* scintillators has been utilized in missions worldwide within areas of scientific research, medical industry, military defense and homeland security. Commercial scintillators are costly with high energy consumption through the sintering. It is of great significance to seek alternative scintillating materials for sensitive X-ray detection in the next-generation. Herein, eight structure-defined Ln(III)-based metal–organic frameworks (Ln-MOFs) were prepared, 2D $[Ln_2(1,4\text{-ndc})_3(DMF)_4]_n \cdot nH_2O$ (Ln = Sm **1**, Eu **2**, Dy **3**, Tb **4**) and 3D $[Ln_4(2,6\text{-ndc})_6(\mu_2\text{-}H_2O)_2(H_2O)_4]_n \cdot 2nH_2O$ (Ln = Sm **5**, Eu **6**, Dy **7**, Tb **8**), where 1,4-H_2ndc = 1,4-naphthalene dicarboxylate acid, 2,6-H_2ndc = 2,6-napthalene dicarboxylate acid, DMF = *N*,*N*-dimethylformamide. Merely compounds **2** and **6** show remarkable X-ray scintillation performance *via* the characteristic red emissions of Eu(III) ions, in which the absorbed energy from the triplet states of the organic moieties can be transferred more efficiently to the resonance emission levels of Eu(III) ions than other lanthanide(III) ions. The X-ray dosage rate detection limits of **2** and **6** are superior to the standard for the medical X-ray diagnosis dosage rate. As proofs-of-concepts, matrix-mixed membranes fabricated with **2** and **6** have achieved remarkable X-ray imaging with high resolution for practical object shooting.

X-ray detection and imaging has been of great essence in medical diagnosis, non-destructive industrial detection, security inspection and other radiation-related fields nowadays [1,2]. The densities and thicknesses of a matter are the decisive factors to the absorption intensity of incident X-ray, in which these features can be employed to find the inside cryptic defects through X-ray imaging [3,4]. In recent decades, great efforts and contributions have been made to improve the quality of X-ray imaging with the reduction of the X-ray exposure [5,6]. Semiconductors like metal halide perovskites, previously applied to solar cells, can be repurposed in X-ray detection and imaging, whose imaging qualities are comparable with those of currently available commercial detectors [7,8]. However, the detection limits of these semiconductors are still poorer than those of the scintillator-based X-ray detectors so far [9,10]. This can be imputed to the baseline drift within semiconductors, which is ineluctably induced by dark current and ion migrations. The baseline drift further increases the shot noise level in turn, resulting in grainy or blurry images to a certain degree [11]. Although hundreds of X-ray scintillators have been reported, dozens of them have been utilized in practice yet [12–14]. These inorganic scintillators are often sintered at a high temperature (>1000 °C) by blending highly purified raw materials and activators, which possibly results in mesoscopic defects and further brings about scintillation quenching [15]. The high cost of construction and harsh synthesis conditions also leads to a long period of creating novel scintillators. Furthermore, the relationship between scintillation performance and structure still remains ambiguous, which is an urgent need for a deep-going comprehension of structure-function relationship for scintillators. Fortunately, scintillating metal–organic frameworks (SMOFs), emerging as a new class of scintillators, have shown great potential applications in X-

* Corresponding authors at: State Key Laboratory of Structural Chemistry, Fujian Institute of Research on the Structure of Matter, Chinese Academy of Sciences, Fuzhou 350002, China
E-mail addresses: lujian@fjirsm.ac.cn (J. Lu), zfk@fjirsm.ac.cn (F. Zheng).

https://doi.org/10.1016/j.cclet.2022.03.085
1001-8417/

ray detection and imaging [16,17]. Unlike lead halide perovskites, in which the components are of great toxicity and vulnerable to heat/light/humidity [18,19], SMOFs are self-assembled *via* inorganic moiety and organic motifs, whose performance and stability could be tailored through artificial regulation, and their various structures could serve as a platform in the sensitive scintillators design and creation [16,20,21]. The previously documented SMOFs mainly are constructed by heavy metal ions or cluster ions like Pb^{2+}, UO_2^{2+}, Ba^{2+} and Zr^{4+}/Hf^{4+} [22,23]. However, uranium is a kind of radioactivity and lead ions are physically toxic. Developing novel SMOFs based on other heavy metal ions seems to be of an urgent desire. To enhance the X-ray attenuation efficiency, SMOFs possessing heavy metal ions with high atomic numbers *Z* are indispensable. The heavy metal effects of lanthanide ions are effective in blocking and absorbing the ionizing X-ray photons, thus making Ln(III)-based SMOFs (Ln-SMOFs) possible in X-ray detection and imaging [24,25]. Nevertheless, the energy transfer pathways have not been clarified so far. It is of great significance to illuminate the energy transfer processes for highly X-ray responsive Ln-SMOFs.

Taking these mentioned above into account, the conjugated naphthalene motifs with π electrons and characteristically emissive lanthanide(III) ions (Sm, Eu, Dy, Tb) were screened to construct a series of lanthanide(III)-based MOFs, 2D $[Ln_2(1,4\text{-ndc})_3(DMF)_4]_n{\cdot}nH_2O$ (Ln = Sm **1**, Eu **2**, Dy **3**, Tb **4**) and 3D $[Ln_4(2,6\text{-ndc})_6(\mu_2\text{-}H_2O)_2(H_2O)_4]_n{\cdot}2nH_2O$ (Ln = Sm **5**, Eu **6**, Dy **7**, Tb **8**), where 1,4-H_2ndc = 1,4-naphthalene dicarboxylate acid, 2,6-H_2ndc = 2,6-napthalene dicarboxylate acid, DMF = *N*,*N*-dimethylformamide. Through detailed spectral characterization, the energy transfer process in the obtained Ln-SMOFs has been explicated clearly. Owing to the higher photosensitized energy transfer efficiency in antenna effects, the X-ray dosage rate detection limits of Eu(III)-based compounds **2** and **6** can reach up to 2.032 $\mu Gy_{air}/s$ and 3.349 $\mu Gy_{air}/s$, respectively, superior to the standard for the medical X-ray diagnosis dosage rate of 5.50 $\mu Gy_{air}/s$. The magnificent X-ray dosage rate detection limits based on the excellent scintillation performance of **2** and **6** have been successfully achieved *via* the Ln-SMOFs. Besides, the high-resolution X-ray imaging has been proofs-of-concepts on basis of **2** and **6** for practical object shooting.

Compounds **1**–**8** were all prepared through solvothermal reactions of $Ln(NO_3)_3{\cdot}6H_2O$ with corresponding naphthalene dicarboxylate ligands, and structurally characterized by single-crystal X-ray diffraction and powdered X-ray diffraction (PXRD). Through PXRD identifications, compounds **1**–**4** are isostructural, and **5**–**8** are of another same structure (Figs. 1a and c) [26–28]. The purities and architectural features of as-synthesized crystalline samples **1**–**4** as well as **5**–**8** were further confirmed by Fourier transform infrared (FT-IR) spectra (Figs. S1 and S2 in Supporting information) and TG&DSC results (Figs. S3 and S4 in Supporting information).

Compounds **1**–**4** all share the triclinic crystallographic system in *P*–1 group. The Sm(III)-based compound **1** was selected as a representative for the structural description of **1**–**4**. In the asymmetric unit of **1**, there contains one Sm^{3+} ion, one full-occupied deprotonated 1,4-ndc^{2-} ligand, one half-occupied 1,4-ndc^{2-} ligand, two coordinated DMF molecules and one half-occupied lattice water molecule. It is worth mentioning that the half-occupied deprotonated 1,4-ndc^{2-} ligand linkers are positional disordered in **1**. As illustrated in Fig. S5 (Supporting information), Sm^{3+} is coordinated by nine oxygen atoms from two DMF molecules, three full-occupied 1,4-ndc^{2-} and two half-occupied 1,4-ndc^{2-}. The nine-coordinated Sm^{3+} demonstrates a geometrical configuration of a mono-capped square-antiprism, with the Sm–O bond lengths ranging from 2.397(6) to 2.678(2) Å. The 1,4-ndc^{2-} ligands display μ_3 (chelating-bridging and chelating) and μ_4 (bidentate bridging and bidentate bridging) different coordination styles (Fig. S6 in Supporting information). These variable carboxylate groups concatenate two adjacent Sm^{3+} ions to result in a centrosymmetric binuclear structure as the secondary building units (SBUs), which are extended infinitely by 1,4-ndc^{2-} in the [1 0 0] and [0 1 0] directions to form a 2D layer parallel to the *ab* plane (Fig. 1b).

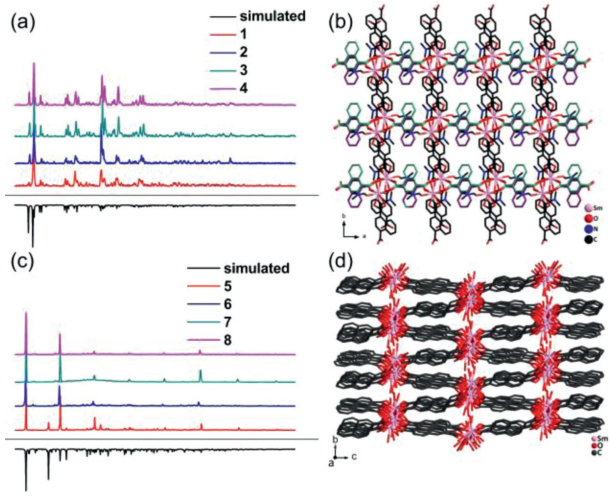

Fig. 1. The powdered X-ray diffraction (PXRD) patterns of compounds **1**–**4** (a). The 2D layer of compounds **1**–**4** parallel to the *ab* plane (b). The powdered X-ray diffraction (PXRD) patterns of compounds **5**–**8** (c). The 3D framework of compounds **5**–**8** (d).

Compounds **5**–**8** all crystallize in the $P2_1/n$ space group. Take the Sm-based compound **5** as a representative example for the structural description of **5**–**8**. In the asymmetric unit of **5**, there are four Sm^{3+} ions, five integrated 2,6-ndc^{2-}, two halved 2,6-ndc^{2-}, two bridging water molecules, four terminate water molecules and two lattice water molecules. The two halved 2,6-ndc^{2-} can be evolved into intact ones through center inversion symmetric operations. As descried in Fig. S7 in Supporting information, these four Sm^{3+} are all coordinated by nine oxygen atoms, with the Sm–O bond lengths varying from 2.356(6) to 2.909(5) Å, further forming the monocapped square antiprism. The 2,6-ndc^{2-} ligands all exhibit a μ_4 coordination mode with different styles. Three different coordination patterns of carboxylate group exist: chelating-bridging and bidentate bridging, chelating-bridging and chelating-bridging, and bidentate bridging and bidentate bridging (Fig. S8 in Supporting information). These four Sm^{3+} are connected one after another by carboxylate groups of deprotonated 2,6-ndc^{2-} ligands to behave as a one-dimensional rod along the *a* axis. The Sm1 and Sm3 ions can form a plicated layer with the 2,6-ndc^{2-}, which is parallel to the *bc* plane. The Sm2 and Sm4 ions can form another rugged layer also parallel to the *bc* plane. These two planes are integrated into a double decker through shared ligands, and further infinitely extended in arrangements by the Sm–O rods along the [1 0 0] direction to produce a 3D framework (Fig. 1d).

The conjugated backbone of polycyclic aromatic hydrocarbons (PAHs) can effectively absorb the energy of exogenous photostimulation and transfer it to the Ln(III) ion centers through the antenna effects, which could effectively resolve the f-f Laporte-forbidden transition [29]. These MOFs have shown remarkable photoluminescence (PL) properties and efficient X-ray detection merits [17,30]. The abundant π-electrons in 1,4-H_2ndc and 2,6-H_2ndc are beneficial in photon harvesting and energy transfer [31]. X-ray stimulated luminescent (XSL) measurement could be employed as an effective method to evaluate the X-ray scintillation performance of radiation detection materials. From the XSL spectra (Fig. S9 in Supporting Information), only compounds **2** and **6** were found to show their characteristic red scintillation.

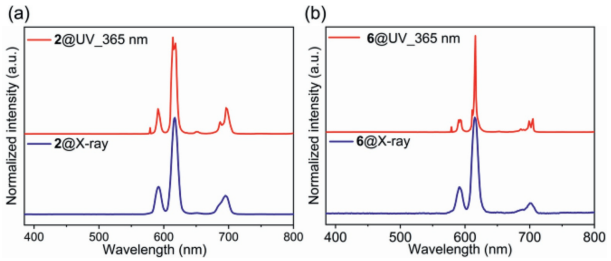

Fig. 2. The photoluminescent (PL) and X-ray stimulated luminescent (XSL) spectra of compounds **2** (a) and **6** (b).

The hand-held UV lamp as well as the PL profiles were also applied to screen the performance of Ln-MOFs **1**–**8**, and sharp red emissions were also observed in **2** and **6** (Fig. S10 in Supporting Information), indicating that **2** and **6** display the higher energy transfer efficiency occurring from the ligands to Eu(III) ions [32]. As shown in Fig. 2, the PL spectrum of **2** exhibits the sharpest characteristic band centered around 614/618 nm ($^5D_0 \rightarrow {}^7F_2$), and other lower peaks at 579/591 ($^5D_0 \rightarrow {}^7F_1$), 651 ($^5D_0 \rightarrow {}^7F_3$) and 687/696 nm ($^5D_0 \rightarrow {}^7F_4$) synchronously, and the dual peaks should be results of the symmetric environment of Eu^{3+}. For **6**, the sharp characteristic emission is very similar to that of **2** due to the same charge transfer process, which is centered around 611/616 nm ($^5D_0 \rightarrow {}^7F_2$), and other lower peaks at 579/592 ($^5D_0 \rightarrow {}^7F_1$), 705 ($^5D_0 \rightarrow {}^7F_3$) and 686/699 nm ($^5D_0 \rightarrow {}^7F_4$). Their XSL spectra just gave rough but broader profiles of full width at half maximum (FWHM), and the main emissions are held at 592/617/695 nm for **2** and 591/615/701 nm for **6** (Fig. 2, Table S3 in Supporting information). This can be ascribed to the ionization and exciton recombination process of these SMOFs upon high energetic X-ray, which will lead to a coarse but similar emission shape in the photoluminescent profiles [33]. Since the emission spectra are very similar either excited by X-ray or UV light, the energy transfer process and phonon dynamics are supposed to be similar. The scintillations strongly depend on the luminescent centers in the scintillators [23].

The scintillation performance of **2** and **6** were further evaluated through the *in situ* XSL characterizations at ambient atmosphere upon gradient dosage intensity. The X-ray flux intensity can be modulated by changing the tube current from 50 μA to 100 μA. The variations in X-ray flux intensity represent different X-ray dosage rates deposited onto the samples. As shown in Figs. 3a and b, compounds **2** and **6** remain their characteristic luminescence, and both exhibit an incremental tendency with the increasing X-ray dosage rates. Picking the highest characteristic emission intensity as the independent variable, the relationships between the dosage rate and scintillation intensity are plotted in Fig. 3c. Fitting these data provide two linear equations, indicating that **2** and **6** show linear scintillation responses towards X-ray dosage rate, and this is a desirable property for scintillation applications. Compared with **6**, the slope value of **2** is more favorable, which highlights more sensitive to X-ray. Using the 3σ rule ($\sigma = S_0/S$, S_0 is known as the standard deviation of the instrumental measurements, and S stands for the slope value of the calibration curve) [34], the limits of detections (LOD) for X-ray dosage rate of **2** and **6** were calculated to be around 2.032 $\mu Gy_{air}/s$ and 3.349 $\mu Gy_{air}/s$, respectively. These LOD values are superior to the standard dosage rate 5.50 $\mu Gy_{air}/s$ for the medical X-ray diagnosis, which indicates that **2** and **6** hold great latent applications in medical diagnosis [35–37]. To well demarcate the high performance of targeted compounds **2** and **6**, the XSL profiles of all reactant species including the commercial powdered scintillators PWO, BGO and LYSO were collected for comprehensive comparison. As depicted in Fig. 3d, it is obviously seen that the reactant materials showed rather weak XSL signals, but when assembled into a coordination complex as an integrity, the scintillation gets significantly improved. The synergistic effects as well as the antenna effects between the organic moieties and inorganic motifs play key roles in designing excellent scintillating Ln(III)-SMOFs. Besides, the scintillation performances of as-synthesized **2** and **6** surpass commercial PWO and BGO, but are less superior to LYSO. X-ray attenuation length (XAL) is another key parameter for measuring the radiation stopping power [38]. Under the radiation lower than ~7.5 keV of X-ray photons, the XAL value remains same for **2** and **6** (Fig. 3e), indicating thicker films around micrometer scale of **2** and **6** are needed for subsequent X-ray imaging experiments. The effective atomic number Z_{eff} can also be applied in evaluating X-ray scintillators [22]. As listed in Table S4 in Supporting information, the Z_{eff} values of **2** and **6** are comparable to other reported SMOFs, indicating their potential applications in sufficient X-ray blocking and scintillation [25]. The scintillation intensity of **2** is around 2.1 times higher than that of **6**. The photoluminescence quantum yield (PLQY) of 1,4-H_2ndc, 2,6-H_2ndc, **2** and **6** were further investigated in the solid state to figure out this phenomenon. The PLQY values of 1,4-H_2ndc and **2** are 6.97% and 34.50%, respectively (Figs. S11a and c in Supporting information), and those of 2,6-H_2ndc and compound **6** are 48.06% and 34.87%, respectively (Figs. S11b and d in Supporting information). The photosensitized energy transfer efficiency of Eu(III) ions can be measured through the PLQY ratio value of ligands and its constructed SMOFs [39]. For **2**, the ratio value is 4.95, larger than 0.73 for **6**. Apparently, the absorbed energy of 1,4-ndc^{2-} is transferred much more efficiently to the constructed compound **2**. It is suggested that the photosensitized efficiency of Eu(III) will determine the characteristic red scintillation performance in **2** and **6**. In particular, the crystal structures and scintillation properties of **2** and **6** show almost no change after X-ray irradiation under a dose of 30 Gy_{air} with at a dose rate of 16.625 mGy_{air}/s for half an hour (Figs. S12 and S13 Supporting Information). The radiation stabilities of **2** and **6** have ensured the possibility of practical application for these Eu-MOFs.

The scintillation and luminescence diversities for the Ln(III) ions constructed compounds root in the energy level matching degree between the triplet energy level of ligands and the resonance emission level of Ln(III) ions [40,41]. The PL spectra of 1,4-H_2ndc/2,6-H_2ndc were recorded at 77 K to evaluate their triplet energy level. As illustrated in Figs. 4a and b, upon excitation at 300/350 nm, the main value of the emission in the phosphorescence spectra is around 504 nm (*ca.* 19,841 cm^{-1}, T_1 state) for 1,4-H_2ndc, and 399/423 nm (*ca.* 25,062 cm^{-1}, T_i state, 23,641 cm^{-1}, T_1 state) for 2,6-H_2ndc. From the emission transition position of common Ln(III) ions, the characteristic resonance emission levels can be determined, which are $^4G_{5/2}$ for Sm^{3+} (18,000 cm^{-1}), $^5D_0$ for Eu^{3+} (17,200 cm^{-1}), $^4F_{9/2}$ for Dy^{3+} (21,000 cm^{-1}), and $^5D_4$ for Tb^{3+} (20,400 cm^{-1}), respectively [39]. The characteristic resonance emission levels of Dy^{3+} and Tb^{3+} are higher than the triplet energy level of ligand 1,4-H_2ndc, making it impossible that **3** and **4** would emit their intrinsic emissions, since the energy process from the ligand to the Dy^{3+} and Tb^{3+} ions is hindered. For **1**, the energy difference (Δ) between the $^4G_{5/2}$ resonance emission level of Sm^{3+} and T_1 energy of 1,4-H_2ndc is 1841 cm^{-1}, and this small gap might grant an energy back transfer (EnBT) process. The energy transferred from the ligand to the Sm^{3+} ions would be reversed to the ligand, weakening the characteristic emissions of Sm^{3+} ions. The Δ value is 2641 cm^{-1} for **2**, larger than that of **1**, which may increase the possibility of energy being transferred from ligand to the metal ions and meanwhile reduce the energy dissipation in the EnBT process.

The same situation also goes for the 2,6-ndc based compounds. The ligand 2,6-H_2ndc bestows a higher excited T_i and T_1 states

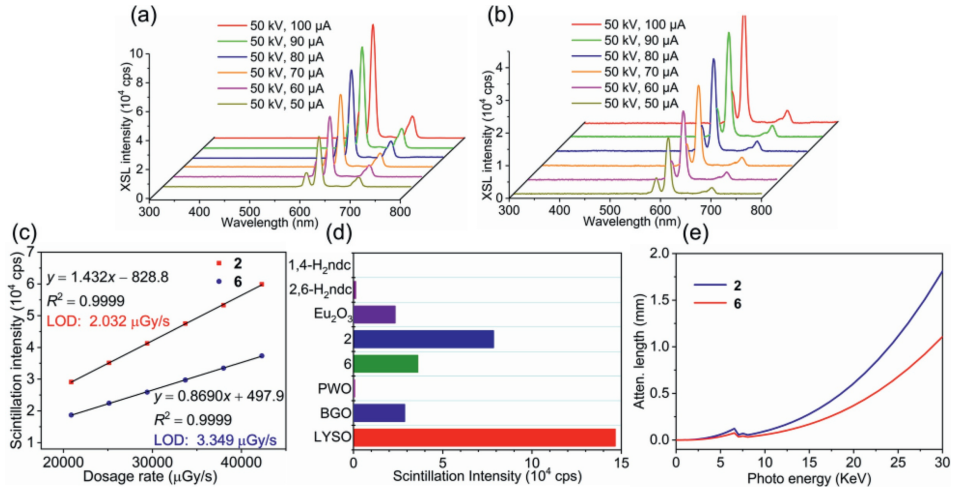

Fig. 3. The XSL spectra of compounds **2** (a) and (b) **6** against X-ray radiation with variable dosage rate. (c) The dose dependence of the XSL intensity and detection limit of compounds **2** and **6**. (d) Comparisons of the XSL signals of related target compounds with powdered PWO, BGO and LYSO as internal references. (e) The X-ray attenuation lengths of compounds **2** and **6**.

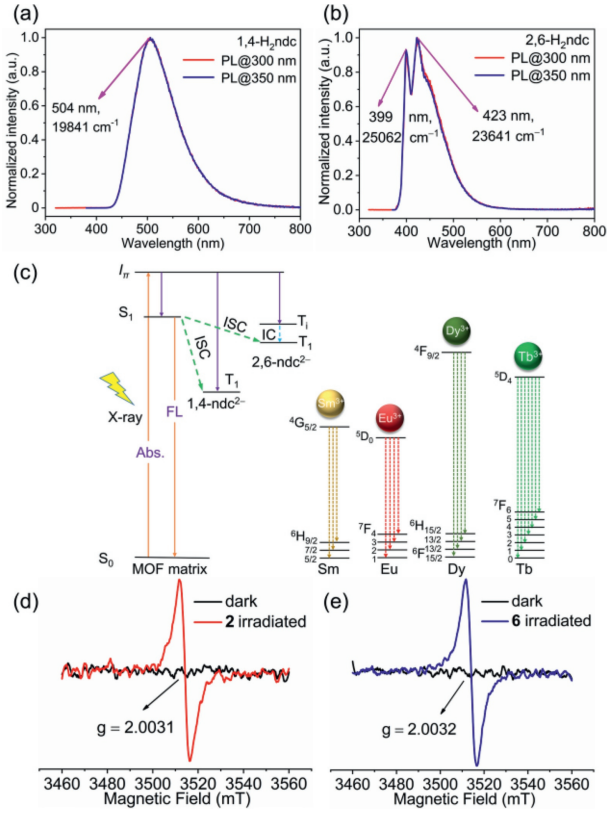

Fig. 4. The phosphorescent spectra of 1,4-H_2ndc (a) and 2,6-H_2ndc (b) at 77 K. (c) The proposal mechanism for the scintillating process. The EPR spectra of compounds **2** (d) and **6** (e) with *g* values of 2.0031 and 2.0032, respectively. Abs. = Absorption, FL = Fluorescence, ISC = Intersystem Crossing, IC = Internal Conversion. The vibrational level of the excited triplet state T_i will undergo fast internal conversion (IC) process to relax to the lowest vibrational level of the T_1 state.

than those of Ln(III) ions, and the differences are 5641 cm^{-1} for Sm^{3+}, 6441 cm^{-1} for Eu^{3+}, 2641 cm^{-1} for Dy^{3+} and 3241 cm^{-1} for Tb^{3+}, respectively. These differences made it possible for the photosentization process. Compounds **5**–**8** all showed their characteristic emissions, but exhibited great imparity in their PL spectra. Compound **6** gave sharp and strong emissions while **5**, **7** and **8** emitted rather weaker characteristic resonance emission but stronger emissions based on the ligands. As clarified in Fig. 4c and Fig. S10 in Supporting Information, the larger difference value seems to give higher energy transfer efficiency. It can be inferred that the energy level of characteristic resonance emission level of Eu^{3+} is well-matched to the T_1 energy level of 1,4-H_2ndc/2,6-H_2ndc ligands, whose LMCT process might be induced to a larger possibility, further leading to the efficient energy transfer. It can also be concluded that the minor difference between the T_1 energy level and characteristic resonance emission level of Ln(III) ions will easily result in the EnBT process, which may weaken the characteristic luminescence of Sm^{3+}, Dy^{3+} and Tb^{3+} ions.

The photosensitized process of compounds **2** and **6** can be identified through *in situ* EPR experiments at room temperature. As shown in Figs. 4d and e, no EPR signal was detected before irradiation. Once upon irradiation, compounds **2** and **6** both generated a sharp single-line signal at the 2.0031 and 2.0032, respectively (Figs. S14a and b in Supporting information). These EPR values are in line with those of typical lanthanide(III) ions [42,43], which suggests that **2** and **6** both suffered the spin flip process in their excited states, indicating that the absorbed energy of ligands 1,4-ndc^{2-}/2,6-ndc^{2-} can be effectively transferred to the Eu(III) ions.

These two Eu(III)-based scintillating compounds can efficiently take over the ionizing X-ray photons and exhibit remarkable characteristic red light (CIE = (0.657, 0.337) for **2**, (0.648, 0.337) for **6** (Fig. S15 in Supporting Information). Additionally, powdered **2** and **6** are stable enough in methyl methacrylate (MMA), whose solution-processable abilities tend to form a mixed matrix membrane (MMM) over a large area up to 36 cm^2 through photocuring reactions, allowing for practical X-ray imaging applications. As proofs-of-concepts experiments, we constructed an X-ray imaging system with a projection configuration (Fig. 5a) using crystalline powdered **2** and **6** as the scintillating MMMs-based screen. In order to well block and absorb the X-ray energy, the thickness of MMMs was set as around 0.2 mm as calculated in Fig. 3e, which is sufficient to block the X-rays around 19 keV. By employing a commercial camera and commercial X-ray source, the prototype X-ray imager can reveal the detailed structural information of a denser matter within a resin outwear (Fig. 5a). The photographs of a spring in the capsule X-ray imaging *via* scintillators **2** and **6** are exhibited in Figs. 5b and c, respectively. The organic masks (*i.e.*, plastic capsule, l_1 23.45 mm $^*\Phi_1$ 7.44 mm), inorganic materials such as spring coil (l_2 26.44 mm $^*\Phi_2$ 4.25 mm, ~0.36 mm in thickness) (Fig. S16 in Supporting information) can be revealed by X-ray without compromising any resolution ability, even the bent 2D shape

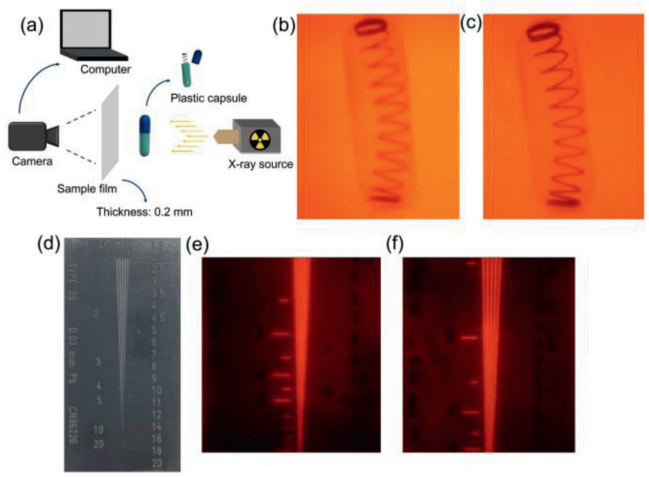

Fig. 5. The diagrammatic sketch of imaging system (a). The photographs of a spring in the capsule X-ray imaging *via* scintillators **2** (b) and **6** (c). The practical line-pair comparison card (d). The practical line-pair comparison card imaged profiles *via* scintillators **2** (e) and **6** (f).

is in good full view (Fig. 5b). The spatial resolution value of X-ray imaging can be evaluated through the line-pair comparison card. The better scintillation performance will grant a higher spatial resolution. Impressively, such a simple prototype is able to provide a spatial resolution as high as 5.5 lp/mm with **2**, which is mainly restricted to the crack virtue of the thin film, and higher than that of 3.0 lp/mm with **6** (Figs. 5d–f). The high resolution is comparable to those of perovskite scintillators [7,44], leaving **2** and **6** as latent commercial scintillating materials in the X-ray imagining market.

In summary, a series of lanthanide(III) based metal–organic frameworks **1**–**8** have been synthesized. Through detailed spectral characterization, the energy transfer process in the obtained Ln(III)-SMOFs has been explicated clearly. Due to the antenna effects, compounds **2** and **6** showed the characteristic red scintillation merits of Eu(III) ions. The characteristic resonance emission level of Eu^{3+} is well-matched to the excited triple state energy level of 1,4-ndc^{2-}/2,6-ndc^{2-} ligands, further resulting in the efficient energy transfer process. Their X-ray dosage rate detection limits can reach up to 2.032 μGy_{air}/s and 3.349 μGy_{air}/s, superior to the standard for the medical X-ray diagnosis dosage rate of 5.50 μGy_{air}/s. Owing to the higher photosensitized energy transfer efficiency from the ligand to Eu^{3+} ions, the scintillation performance of **2** is superior to **6**. The application prospects of Ln(III)-SMOFs have also been explored, and the high-resolution X-ray imaging has been proofs-of-concepts based on the excellent scintillation performance of **2** and **6** for practical object shooting. This work has provided a theoretical and experimental strategy for designing lanthanide(III)-based X-ray scintillation MOFs, which will guide a superior and competitive trend for future X-ray imaging *via* scintillating MOFs.

Declaration of competing interest

The authors declare that they have no known competing financial interests or personal relationships that could have appeared to influence the work reported in this paper.

Acknowledgments

This work was supported by the National Natural Science Foundation of China (Nos. 21971240 and 21827813), the National Key R&D Program of China (No. 2017YFA0206802), and the Strategic Priority Research Program of the Chinese Academy of Sciences (No. XDB20000000).

Supplementary materials

Supplementary material associated with this article can be found, in the online version, at doi:10.1016/j.cclet.2022.03.085.

References

[1] Y.C. Liu, Z. Xu, Z. Yang, et al., Matter 3 (2020) 180–196.
[2] H. Zhang, Z. Yang, M. Zhou, et al., Adv. Mater. 33 (2021) 2102529.
[3] L. Lu, M.Z. Sun, Q.Y. Lu, T. Wu, B.L. Huang, Nano Energy 79 (2021) 105437.
[4] Y.H. He, C.C. Stoumpos, I. Hadar, et al., J. Am. Chem. Soc. 143 (2021) 2068–2077.
[5] Y.C. Liu, Y.X. Zhang, X.J. Zhu, et al., Adv. Mater. 33 (2021) 2006010.
[6] J.A. Rowlands, Nature 550 (2017) 47–48.
[7] Y.C. Kim, K.H. Kim, D.Y. Son, et al., Nature 550 (2017) 87–91.
[8] Q.S. Hu, Z.Z. Deng, M. Hu, et al., Sci. China Chem. 61 (2018) 1581–1586.
[9] J.J. Zhao, L. Zhao, Y.H. Deng, et al., Nat. Photon. 14 (2020) 612–617.
[10] C.Y. Liang, S.T. Zhang, L.W. Cheng, et al., Angew. Chem. 132 (2020) 11954–11958.
[11] G.J. Matt, I. Levchuk, J. Knüttel, et al., Adv. Mater. Interfaces 7 (2020) 1901575.
[12] C.W.E. van Eijk, Phys. Med. Biol. 47 (2002) 85–106.
[13] F. Maddalena, L. Tjahjana, A.Z. Xie, et al., Crystals 9 (2019) 88–116.
[14] H.A. Höppe, Angew. Chem. Int. Ed. 48 (2009) 3572–3582.
[15] G.G. Li, J. Lin, Chem. Soc. Rev. 43 (2014) 7099–7131.
[16] F.P. Doty, C.A. Bauer, A.J. Skulan, P.G. Grant, M.D. Allendorf, Adv. Mater. 21 (2009) 95–101.
[17] J. Lu, J. Gao, W.F. Wang, et al., J. Mater. Chem. C 9 (2021) 5615–5620.
[18] B. Yang, L.X. Yin, G.D. Niu, et al., Adv. Mater. 31 (2019) 1904711.
[19] F. Yang, A.C. Wang, S. Yue, et al., Sci. China Mater. 64 (2021) 2889–2914.
[20] L.W. Cheng, C.Y. Liang, W. Liu, et al., J. Am. Chem. Soc. 142 (2020) 16218–16222.
[21] V. Villemot, N. Dufour, S. Mauree, et al., Adv. Photon. Res. 3 (2021) 2100259.
[22] J. Lu, X.H. Xin, Y.J. Lin, et al., Dalton Trans. 48 (2019) 1722–1731.
[23] Y.X. Wang, X.M. Yin, W. Liu, et al., Angew. Chem. Int. Ed. 57 (2018) 7883–7887.
[24] A.A. Kukinov, T.V. Balashova, V.A. Ilichev, et al., Phys. Chem. Chem. Phys. 21 (2019) 16288–16292.
[25] X. Wang, Y.X. Wang, Y.L. Wang, et al., Chem. Commun. 56 (2020) 233–236.
[26] O. Karagiaridi, W. Bury, A.A. Sarjeant, et al., Chem. Sci. 3 (2012) 3256–3260.
[27] N.A. Khan, M.M. Haque, S.H. Jhung, Eur. J. Inorg. Chem. 31 (2010) 4975–4981.
[28] Z.J. Lin, R.Q. Zou, W. Xia, et al., J. Mater. Chem. 22 (2012) 21076–21084.
[29] T.C. Sun, R.Q. Fan, R. Xiao, et al., J. Mater. Chem. A 8 (2020) 5587–5594.
[30] J. Lu, X.H. Zhao, B. Bai, F.K. Zheng, G.C. Guo, J. Mater. Chem. C 7 (2019) 11099–11103.
[31] H. Li, L.Y. Wang, ACS Appl. Mater. Interfaces 5 (2013) 10502–10509.
[32] Y. Xiao, S.H. Wang, F.K. Zheng, et al., CrystEngComm 18 (2016) 721–727.
[33] J. Lu, H.F. Wu, W.F. Wang, et al., Chem. Commun. 55 (2019) 13816–13819.
[34] W.C. Pan, H.D. Wu, J.J. Luo, et al., Nat. Photon. 11 (2017) 726–732.
[35] Q.Q. He, C.K. Zhou, L.J. Xu, et al., ACS Mater. Lett. 2 (2020) 633–638.
[36] D.R. Shearer, M. Bopaiah, Health Phys. 79 (2000) 20–21.
[37] S.J. Tie, W. Zhao, D.Y. Xin, et al., Adv. Mater. 32 (2020) 2001981.
[38] Y.X. Wang, Y.M. Wang, X. Dai, et al., Inorg. Chem. 58 (2019) 2807–2812.
[39] K. Miyata, Highly Luminescent Lanthanide Complexes with Specific Coordination Structures, Hokkaido University, JapanSapporo, 2014.
[40] É. Whelan, F.W. Steuber, T. Gunnlaugsson, W. Schmitt, Coord. Chem. Rev. 437 (2021) 213757–213780.
[41] J.W. Wu, H.B. Zhang, S.W. Du, J. Mater. Chem. C 4 (2016) 3364–3374.
[42] F. Avecilla, C. Platas-Iglesias, R. Rodríguez-Cortiñas, et al., J. Chem. Soc. Dalton Trans. 24 (2002) 4658–4665.
[43] J.E. McPeak, S.S. Eaton, G.R. Eaton, Methods Enzymol. 651 (2021) 63–101.
[44] Y.H. Zhang, R.J. Sun, X.Y. Ou, et al., ACS Nano 13 (2019) 2520–2525.